

# Multiscale optical flow probing of dynamics in solar EUV images

## Algorithm, calibration, and first results

S. F. Gissot<sup>1,2</sup> and J.-F. Hochedez<sup>1</sup>

<sup>1</sup> Solar Influences Data analysis Centre, Royal Observatory of Belgium, Avenue Circulaire 3, 1180 Brussels, Belgium  
e-mail: [samuel.gissot;hochedez]@sidc.be

<sup>2</sup> Unité de Physique Théorique et de Physique Mathématique – FYMA, Université catholique de Louvain, Chemin du Cyclotron 2, 1348 Louvain-la-Neuve, Belgium

Received 5 May 2006 / Accepted 24 October 2006

### ABSTRACT

**Context.** Movies of the solar atmosphere reveal motion and variations in brightness. In particular, sequences of coronal images exhibit the plane-of-the-sky component of the velocity combined with other variations in the signal. The present work analyses solar extreme-ultraviolet images, as recorded by the Extreme ultraviolet Imaging Telescope (EIT) on board the Solar and Heliospheric Observatory (SoHO) and by the Transition Region and Coronal Explorer (TRACE).

**Aims.** Our aim is to simultaneously estimate the apparent motion vector and the variation in brightness from two successive images.

**Methods.** We present a multiscale optical-flow algorithm derived from a local gradient-based technique that estimates the deformation parameters. Our algorithm is symmetric in the sense that it computes the exact same estimation if the two images are swapped. This also regularises the optical flow when two local image patterns do not match, e.g. in case of temporal sub-sampling. Independently our algorithm regularises the optical flow against aperture effects occurring typically along coronal loops.

**Results.** We demonstrate a new differential rotation measurement technique and the identification of coronal events as regions exhibiting a significant brightness variation or an outstanding velocity field. Space weather services have motivated this study. The range of potential interests includes, but also extends beyond, on-disc signatures of flares and coronal mass ejection (CME). It encompasses, for example, studies of bright points and filaments, coronal seismology, and EIT wave investigations.

**Key words.** methods: numerical – Sun: corona – Sun: activity – Sun: rotation – techniques: image processing – Sun: UV radiation

## 1. Introduction

The dynamic nature of the solar atmosphere has been widely observed and modelled (e.g. Moses et al. 1997; Schrijver et al. 1999; Peter et al. 2006). Recent years have highlighted the unsuitability of static assumptions in studying the physics of the chromosphere, transition region, and corona. The probe of dynamics is concerned with the effects of forces upon motion, and reciprocally, the knowledge of motions and accelerations must constrain the models, consequently validating or falsifying the underlying physics. While forces are invisible, motion can be quantitatively estimated by observational means, and both spectroscopy and image sequences can reveal motion. Spectroscopy informs on the line-of-sight (LOS) velocity component for travelling plasma, while movies exhibit the transversal component of the speed. Both approaches have their respective advantages and restrictions, but they are complementary when the two types of observations coincide (e.g. Kucera et al. 2003). The present work deals only with the second approach, focusing specifically on solar extreme ultraviolet (EUV) images as produced by EIT (Delaboudinière et al. 1995) on board SoHO, TRACE (Handy et al. 1999), or SPIRIT-CORONAS (Oraevsky & Sobelman 2002). However these developments have potential for application to magnetographic, photospheric, and coronographic image sequences or future observations from EUV imagers PROBA2-SWAP, SDO-AIA, or STEREO-SECCHI.

Introducing the concept of *apparent motion* immediately states a fundamental limitation of imaging data: images are

projections of the sky of 3D features in the 2D plane. This problem of perspective in the mostly transparent corona corresponds not only to geometrical distortions of the velocity fields but also to ambiguities, if more than one “feature” superimpose on the LOS. It also generates occultations where opaque objects, such as prominences or the solar disc itself, are considered. However, the issue of apparent motion goes beyond projection effects alone: motion tracking algorithms, as well as human observers, can trace only intensity patterns but not actual plasma elements. Without spectroscopic information, propagating brightness patterns are a priori indistinguishable from actual motions (De Groof et al. 2004). Fortunately, at the same time, this ambiguity gives access to a range of phenomena able to bring physical insights of their own (e.g. Deforest & Gurman 1998; Klimchuk et al. 2004). For example, Noglik et al. (2005) calculate the reconnection rate from the estimated velocity at which successive loops brighten.

Nevertheless, solar rotation dominates the motion in image sequences. Recent works (e.g. Brajša et al. 2001; Vršnak et al. 2003) have studied differential rotation of the atmosphere, and the present paper uses their results for comparison. In a future publication, the method will be used for studying the solar rotation over long periods. After differential rotation compensation, the residual motion yields a wealth of insights. Coronal activity is obviously not limited simply to topological evolutions and rearrangements. Temperature variations are ubiquitous, and when they coincide with instrumental passbands, the observed volumes of plasma brighten or darken. As long as too few

bandpasses are recorded, the differential emission measure (DEM) cannot be recovered and it is necessary to separate motion from brightness variations (BV). We show the required conditions for this disentanglement in Sect. 2.2.5.

Estimating both speed and brightness variations in parallel is mathematically logical and also physically meaningful since solar activity exhibits motion, brightening or flaring, and dimming effects. A technique capable of producing velocity and BV maps addresses essentially all phenomena seen in imaging data. Space weather services have motivated this study (e.g. Hochedez et al. 2005), but the range of potential interests extends beyond early warnings of flares and coronal mass ejection (CME) onsets. It includes, for example, studies of bright points and filaments, coronal seismology, EIT wave investigations, etc.

Improving the forecast of geomagnetic disturbances from solar observations is a task of space weather forecast centres. In the low corona, CME onset signatures include filament eruptions, coronal dimmings, EIT waves, loop openings, post-eruption arcades observed in the EUV, and sigmoid-to-arcade restructuring in soft X-rays (Hudson & Cliver 2001). Unfortunately, image processing of solar EUV image sequences is difficult. The main problems stem from noise, the variations in source brightness discussed above, rapid and hence under-sampled topological changes, the lack of spatial resolution (spatial aliasing), and transparency.

There are three main classes of methods for motion analysis of a sequence of *two* images (Barron et al. 1992): gradient-based (local or global), matching-based, and feature-based. Gradient-based and matching-based, such as local correlation tracking (LCT) are said to be *dense*, in contrast to feature-based methods, in the sense that they estimate the velocity at every pixel and not only at sparse features. Dense does not mean that the quality of the estimation is uniform over the image, and we expect that some regions will have better estimations if motion is better defined at these locations. In feature-based methods, the extraction of the features is a problematic preprocessing step. Some authors have proposed matching techniques based on the LCT for sequences of photospheric images (November & Simon 1988; Welsch et al. 2004). This technique has also been modified by Roudier et al. (1999) and applied to TRACE photospheric data (see Krijger et al. 2002; Krijger & Roudier 2003). In order to process vector magnetograms, Longcope (2004) estimates the velocity by minimising an energy term, and their “minimum energy fit” enforces consistency with the magnetic induction equation. All these techniques deal with photospheric velocity flows. Note that the present study does *not* incorporate any physical assumption, but instead utilises *only* the information found in the two images.

To our knowledge and apart from our early publication (Gissot et al. 2003), dense velocity field estimations have not been calculated from EUV sequences of the corona. Brajša et al. (2001) uses a feature-based method to track bright points and point-like structures (PLS), where each feature is a point in the  $(B, \omega_{\text{rot}})$  plane, with  $B$  the heliospheric latitude and  $\omega_{\text{rot}}$  the angular velocity. The authors then fit a parametric model of differential rotation through the cloud of feature points. This method is sensitive to the reliability of the feature extraction.

Here, we present a multiscale optical flow (OF) algorithm derived from the local gradient-based technique of Lucas & Kanade (1981), which we refer to as LK. Our algorithm is *symmetric* (see Sect. 2.2.3), and regularised against aperture effects (see Sect. 2.2.6). Our aim is to estimate both the fields of apparent displacement and brightness variation from two successive images. We further demonstrate a new differential rotation

measurement and identify coronal events as outliers to the differential rotation or as regions exhibiting a significant BV. We apply the algorithm to EIT sequences of May 3, 1998 and April 17, 1999. The paper is organised as follows: in Sect. 2, we present the formulation of our new method of motion analysis. In Sect. 3, we show the results of the calibration of the method on synthetic signals. We finally discuss the analysis of solar observations in Sect. 4.

## 2. Formulation of the method

In order to calculate the coordinates of the velocity vector for each pixel, we establish the optical flow (OF) equations using the brightness constancy assumption (BCA). The BCA (Horn & Schunck 1981) states that the source of intensity remains constant over time. This provides a single equation per pixel – the optical flow constraint equation (OFCE) – while there are two unknowns, namely the two velocity vector coordinates. This is the *aperture problem*. To solve this under-determination, following Lucas & Kanade (1981), we further assume a local uniformity of the velocity field in the neighbourhood of the estimation. An alternative approach would be to solve globally the velocity field (Horn & Schunck 1981) by adding a constraint on its smoothness. The disadvantage of this latter method is that bad estimations can propagate to the rest of the image. Furthermore, a local diagnostic of the quality of the estimation would be impossible when the solution is global. Other important approaches to optical flow computation are probabilistic (Simoncelli et al. 1991; Simoncelli 1999) or robust minimisation (Black & Anandan 1993).

In the sequel, we extend the optical flow to estimate both the velocity and brightness variation ( $\delta I$ ) fields in the special case of coronal ultraviolet images. A *multiscale* computation of the flow iterates the estimation from larger to smaller scales, the scale being associated to the size of the neighbourhood where the least-square estimation is performed. The estimation is updated across scales, along with its *quality* index, as defined in Sect. 2.2.5, used for error prediction (see Sect. 3.1). In the present section, after describing the preprocessing that we apply to the images (Sect. 2.1), we introduce the symmetric optical flow equations (SOFA, see Sect. 2.2.3). It induces a symmetry constraint between the first and the second images, and we interpret this constraint in the Bayesian framework.

### 2.1. Sequence preprocessing

First, we remove the cosmic ray hits (CRH) using a median filter (procedures are part of the solar soft library). We then apply a logarithmic transform to bring out the low-intensity part of the signal. Thirdly, we smooth the image using a Gaussian kernel. This step allows us to compute robust spatial gradient estimations. Thus, if  $g$  is the Gaussian kernel of our smoothing, of bandwidth  $a$ , we denote the preprocessed image  $I_{\text{preprocessed}} = g_a \star I_{\text{raw}}$ . The spatial derivative along  $x$  (same along  $y$ ) is

$$\frac{\partial I_{\text{preprocessed}}}{\partial x} = \frac{\partial}{\partial x}(g_a \star I) = \frac{\partial g_a}{\partial x} \star I. \quad (1)$$

We have access to an analytical derivative of the preprocessed signal  $I = g_a \star I$  where  $a$  is the scale of the Gaussian function  $g_a(x) = \frac{1}{2\pi a^2} \exp(-\frac{x^2}{2a^2})$ . In the rest of this paper, we do not recall this preprocessing and only refer to  $I$ . We choose a scale  $a = 2$  pixels so that it does not filter the images too much. The subscripts  $x$  and  $y$  in  $I_x$  or  $I_y$  designate the partial derivative with respect to  $x$  or  $y$ .

## 2.2. The optical flow equations

There are two equivalent formulations of the OFCE: partial differential equation (PDE) and image registration. We aim at estimating the deformation, if it is “small enough”, between the first image  $I_1$  and the second  $I_2$ . The PDE formulation can be found in Appendix A.

### 2.2.1. Image registration

We denote  $\mathbf{x} = (x, y)^T$ , the spatial position in the image plane (plane-of-the-sky). We can formulate the BCA as

$$I_2(\mathbf{x} + \delta\mathbf{x}) - I_1(\mathbf{x}) = 0. \quad (2)$$

A linear approximation of this equation, using a Taylor series at the first order on the left hand side, gives

$$\nabla I_2 \cdot \delta\mathbf{x} + I_2(\mathbf{x}) - I_1(\mathbf{x}) = \xi(\mathbf{x}, \delta\mathbf{x}), \quad (3)$$

which leads to a formula similar to (A.3). This formulation, where the time variable does not appear explicitly, is used by Lucas & Kanade (1981). The motion vector can then be defined as  $\mathbf{v} = \delta\mathbf{x}/\delta t$ , where  $\delta t$  is the time difference between the two images  $I_1$  and  $I_2$ . This approach leads to the same equation as the PDE formulation (see Sect. A in appendix), so that in practice they are equivalent.

### 2.2.2. Solutions of OF equations

In the original Lucas & Kanade (1981) optical flow estimation, in order to solve the aperture problem, a local uniformity assumption (LUA) is imposed on the velocity vector:  $\mathbf{v}$  has to be uniform over a local neighbourhood (see Fig. 1). The set of OFCE equations in this neighbourhood  $\Omega$  yields a linear system, where the unknowns are the two parameters of the deformation (the motion vector). If  $\Omega(\mathbf{x})$  (centred on  $\mathbf{x}$ ) contains  $N > 2$  pixels, this assumption provides more equations of type (3) than unknowns  $\delta x_i$  so that the linear system is overdetermined and can be solved using a weighted linear least-square method (Press et al. 1992). The local uniformity assumption means that one imposes Eq. (3) in such a way as to be true locally around location  $\mathbf{x}$ , which is over a finite domain neighbourhood  $\Omega(\mathbf{x})$ . The LK optical flow is the least-square minimiser of  $\xi$  in (3) on  $\Omega$

$$\hat{\delta\mathbf{x}}(\mathbf{x}) = \arg \min_{\delta\mathbf{x}} \|\xi(\delta\mathbf{x})\|_{\Omega(\mathbf{x})}^2, \quad (4)$$

where  $\|\xi(\delta\mathbf{x})\|_{\Omega(\mathbf{x})} = (\sum_{i=1}^N \xi(\mathbf{x}_i, \delta\mathbf{x})^2)^{1/2}$  is the Euclidean norm on  $\mathbb{R}^N$  of  $\xi$ . This solution is the maximum likelihood estimator when the residual term  $\xi$  is a random variable following a Gaussian distribution  $N(0, \sigma_\xi^2)$ . In fact, we assign weights to each pixel, or equivalently to each optical flow equation in the neighbourhood  $\Omega(\mathbf{x})$ , so that the pixel at the centre has a greater statistical weight than at the boundaries of  $\Omega(\mathbf{x})$ . The minimising vector defined in Eq. (4) is the solution of the normal equation  $A^T A \delta\mathbf{x} = A^T b$ , where

$$A = \begin{bmatrix} I_{2x}(\mathbf{x}_1) & I_{2y}(\mathbf{x}_1) \\ \vdots & \vdots \\ I_{2x}(\mathbf{x}_N) & I_{2y}(\mathbf{x}_N) \end{bmatrix},$$

$$b = \begin{bmatrix} -(I_2 - I_1)(\mathbf{x}_1) \\ \vdots \\ -(I_2 - I_1)(\mathbf{x}_N) \end{bmatrix}.$$

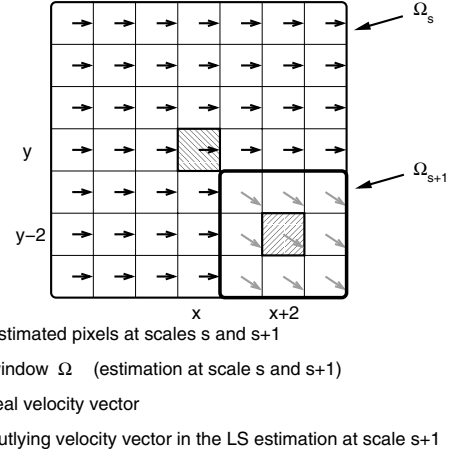


**Fig. 1.** The local uniformity assumption in the multiscale estimation process with an update between scale  $s + 1$  and scale  $s$ . In the lower right corner, the estimation at location  $(x + 2, y - 2)$ , and the quality  $Q$  will be updated (see Sect. 2.2.5).

When the matrix  $A^T A$  is invertible, the solution is

$$\hat{\delta\mathbf{x}} = (A^T A)^{-1} A^T b. \quad (5)$$

We denote  $V_\xi = \sigma_\xi^2 I$ , the covariance matrix of the residual error  $\xi$ . The covariance matrix of  $\hat{\delta\mathbf{x}}$  is then given by

$$V_{\hat{\delta\mathbf{x}}} = (A^T V_\xi^{-1} A)^{-1}. \quad (6)$$

In the rest of this paper, we refer to this covariance matrix as  $V_{\hat{\delta\mathbf{x}}}$  and use it to define our criterion for the quality of the estimation.

### 2.2.3. Symmetric optical flow analysis (SOFA)

We opt for a symmetric formulation of the optical flow, and this generates a stabilising constraint on the flow  $\delta\mathbf{x}$ . To impose symmetry in the optical flow estimation, we combine the two reciprocal equations

$$I_2(\mathbf{x} + (\delta\mathbf{x} + \delta\mathbf{x}_{\text{th}})) = I_1(\mathbf{x}),$$

$$I_1(\mathbf{x} - (\delta\mathbf{x} + \delta\mathbf{x}_{\text{th}})) = I_2(\mathbf{x}).$$

We linearise both equations assuming that  $\delta\mathbf{x}_{\text{th}} = \mathbf{0}$ . It is possible to impose a predetermined  $\delta\mathbf{x}_{\text{th}}$ , for instance the theoretical differential rotation or the estimate on a larger scale as below. We get

$$\nabla I_2 \cdot \delta\mathbf{x} + I_2(\mathbf{x}) - I_1(\mathbf{x}) = \xi_1, \quad (7)$$

$$\nabla I_1 \cdot \delta\mathbf{x} + I_2(\mathbf{x}) - I_1(\mathbf{x}) = \xi_2. \quad (8)$$

We denote  $I_m$  the mean image and  $I_d$  the difference image

$$I_m = \frac{I_1 + I_2}{2} \text{ (mean),}$$

$$I_d = I_2 - I_1 \text{ (difference).}$$

Adding and subtracting (7) and (8), we obtain

$$2 \times (\nabla I_m \cdot \delta\mathbf{x} + I_d(\mathbf{x})) = \xi_1 + \xi_2, \quad (9)$$

$$\nabla I_d \cdot \delta\mathbf{x} = \xi_1 - \xi_2. \quad (10)$$

The goal of the algorithm is now to minimise a redefined cost function  $\|\xi\|^2$ , using the parallelogram identity, as

$$\|\xi\|^2 = \frac{1}{2} (\|\xi_1\|^2 + \|\xi_2\|^2) = \left\| \frac{\xi_1 + \xi_2}{2} \right\|^2 + \left\| \frac{\xi_1 - \xi_2}{2} \right\|^2. \quad (11)$$

We denote  $\hat{\delta\mathbf{x}}$  the vector that minimises the quantity  $\|\xi(\delta\mathbf{x})\|_{\Omega}^2$ . We can interpret this new minimisation either as a generalised Tikhonov regularisation or in the Bayesian framework. The advantage of this method is that the regularisation constraint is derived from the data (the matrix  $M$ ) and does not require any extra arbitrary parameter. Furthermore, the estimation is symmetric: the parameters that minimise  $\|\xi\|^2$  are not dependent on the ordering between  $I_1$  and  $I_2$ . We define

$$A = \begin{bmatrix} I_{m,x}(\mathbf{x}_1) & I_{m,y}(\mathbf{x}_1) \\ \vdots & \vdots \\ I_{m,x}(\mathbf{x}_N) & I_{m,y}(\mathbf{x}_N) \end{bmatrix},$$

$$b = \begin{bmatrix} -I_d(\mathbf{x}_1) \\ \vdots \\ -I_d(\mathbf{x}_N) \end{bmatrix},$$

$$M = \frac{1}{2} \begin{bmatrix} I_{d,x}(\mathbf{x}_1) & I_{d,y}(\mathbf{x}_1) \\ \vdots & \vdots \\ I_{d,x}(\mathbf{x}_N) & I_{d,y}(\mathbf{x}_N) \end{bmatrix}.$$

The cost function  $\|\xi\|^2$  can be written as

$$\|\xi\|^2 = \frac{1}{2} \left( \|A\delta\mathbf{x} - b\|^2 + \|M\delta\mathbf{x}\|^2 \right) \\ \frac{1}{2} \left( \|A\delta\mathbf{x} - b\|^2 + \|\delta\mathbf{x}\|_{M^T M}^2 \right).$$

In the Bayesian framework, it appears that imposing the symmetry is equivalent to adding a prior constraint to the vector  $\delta\mathbf{x}$ . Using Bayes' rule, we interpret Eq. (11) as the following conditional probability

$$\Pr(\delta\mathbf{x}|I_d) = \frac{\Pr(I_d|\delta\mathbf{x}) \times \Pr(\delta\mathbf{x})}{\Pr(I_d)}, \quad (12)$$

where

$$\Pr(I_d|\delta\mathbf{x}) \propto \exp\left(-\frac{1}{2}\delta\mathbf{x}^T V_{\xi}^{-1} \delta\mathbf{x}\right), \quad (13)$$

$$\Pr(\delta\mathbf{x}) \propto \exp\left(-\frac{1}{2}\delta\mathbf{x}^T (M^T V_{\xi}^{-1} M) \delta\mathbf{x}\right). \quad (14)$$

Indeed Eq. (10) can be used to define a prior distribution on  $\delta\mathbf{x}$ . This prior distribution plays a role when the gradient texture is deformed, and the two diagonal elements  $M^T M$  then represent the deformation rates along the  $x$  and  $y$  axes. When the gradient texture is deformed between  $I_1$  and  $I_2$ , because of occlusion or strong deformation, then the estimation is forced to tend to the displacement vector used to linearise the model (here  $\mathbf{0}$  vector, but it could be e.g. the differential rotation). Basically, it stabilises the estimation towards the reference value when the gradient texture is modified between  $I_1$  and  $I_2$ . Finally, we get the solution

$$\hat{\delta\mathbf{x}} = (A^T A + M^T M)^{-1} A^T b. \quad (15)$$

The covariance matrix of  $\delta\mathbf{x}$  is

$$V_{\hat{\delta\mathbf{x}}, \text{sym}} = (A^T V_{\xi}^{-1} A + M^T V_{\xi}^{-1} M)^{-1}.$$

#### 2.2.4. Brightness variation estimation and weights

We extend the OFCE with  $\delta I$ , which estimates the brightness variation between the two images, relaxing the BCA assumption. This approach was suggested by Lucas & Kanade (1981)

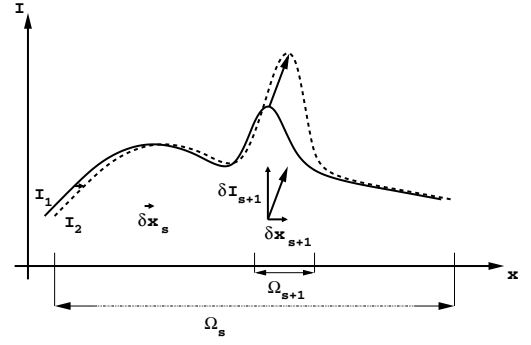


**Fig. 2.** In this 1D example, the estimation is locally updated in motion and brightness variation from scale  $s$  to  $s + 1$ .

and recently used by several authors (e.g. Odobez & Bouthemy 1995; Periaswamy & Farid 2003). An example of a 1D signal undergoing a translation plus a brightness variation is shown in Fig. 2. The BV map can be interpreted as the variation in the LOS emission parameters (temperature and density).

In addition to this extension, we weight each pixel equation within the neighbourhood  $\Omega$  using a function  $w$  to penalise the pixels that are far from the estimated pixel  $\mathbf{x}$ , avoiding a “square paving” effect. The symmetric optical flow Eq. (9) becomes

$$w_i \cdot (\nabla I_m \cdot \delta\mathbf{x} + I_d + \alpha \cdot \delta I) = \xi(\mathbf{x}, \delta\mathbf{x}), \quad (16)$$

but Eq. (10) remains unchanged (except for the weights  $w_i$ ). The  $\alpha$  parameter is used to define  $\delta I$  in the same unit as  $\delta x$  and  $\delta y$ . Our set of weights  $w_i$  penalise the pixels of the neighbourhood  $\Omega$  that are far from the pixel where the parameter set has to be estimated. They are weighted so that

$$\sum_{x_i \in \Omega} w_i^2 = 1.$$

In order to make the maps  $(\delta x, \delta y)$ , which corresponds to the velocity vector map, and  $\delta I$  as local as possible, we compute the optical flow in a multiscale framework (see Figs. 1 and 3). The scale is defined by the scale parameter  $s$  of the Gaussian kernel associated to  $\Omega$ . The first computation is carried out on a pre-defined large scale  $s_0$ . On this scale, a large number of pixels are used in the estimation, which therefore increases its significance. This estimation may nevertheless be biased. Furthermore, within a large neighbourhood (i.e. large scale), the hypothesis made on the optical flow (extended BCA and LUA) is less valid. To compensate for this effect, we add a multiscale updating step. It consists in an update of the parameter estimation from larger to smaller scales. This is explained in Sect. 2.2.7.

From now on, we note the vector to estimate in the space of parameters

$$\hat{\boldsymbol{\theta}} = (\delta x, \delta y, \delta I).$$

The solution becomes

$$\hat{\boldsymbol{\theta}} = (A^T A + M^T M)^{-1} A^T b. \quad (17)$$

The covariance matrix of  $\boldsymbol{\theta}$  is

$$V_{\hat{\boldsymbol{\theta}}, \text{sym}} = (A^T V_{\xi}^{-1} A + M^T V_{\xi}^{-1} M)^{-1}.$$

#### 2.2.5. Quality criterion of estimation

Contrary to global methods such as in Horn & Schunck (1981), our optical flow approach gives the possibility of carrying out the

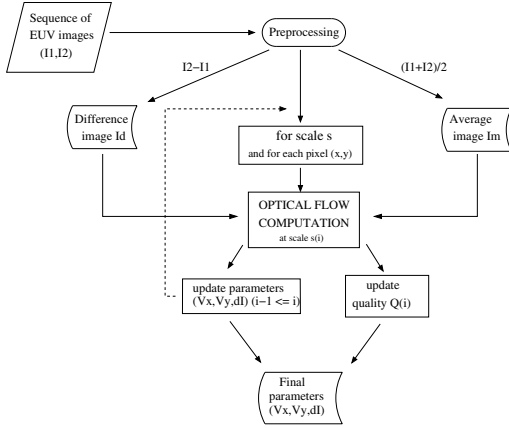


Fig. 3. Overview of the motion analysis algorithm.

registration depending on the neighbourhood content. For that reason, we define an index  $Q$  (for “quality”). We use this index for error prediction of the estimation. In order to illustrate the meaning of  $Q$ , we can use the space of parameter  $(\delta x, \delta y, \delta I)$ . If we assume  $V_\xi = \sigma_\xi^2 I$  and since  $A^T A$  is symmetric, we can write  $A^T A = P^T D' P$ , or  $A^T A + M^T M = P^T D' P$  in the symmetric case, where  $P^T = P^{-1}$ . Equivalently, we have

$$V_{\delta\theta} = P D P^T$$

$$\text{where } D = \begin{bmatrix} \sigma_\xi^2 / \lambda_1 & & \\ & \sigma_\xi^2 / \lambda_2 & \\ & & \sigma_\xi^2 / \lambda_3 \end{bmatrix} = \sigma_\xi^2 D'^{-1}$$

and  $\lambda_1 < \lambda_2 < \lambda_3$ .

We denote  $\mathbf{p}_i$  as the eigenvectors of the matrix  $V_{\delta\theta}$ , which are the columns of the matrix  $P = (\mathbf{p}_1 \mathbf{p}_2 \mathbf{p}_3)$ . Our solution can be written as

$$\hat{\theta} = \hat{\theta}_1 \mathbf{p}_1 + \hat{\theta}_2 \mathbf{p}_2 + \hat{\theta}_3 \mathbf{p}_3. \quad (18)$$

We then define our quality index as:

$$Q = \frac{(\prod_i \lambda_i)^{1/3}}{\sigma_\xi^2}.$$

It is correct to interpret  $Q^{-1}$  as the variance around the estimated vector  $\theta$ . We will see that the aperture reduction (see Sect. 2.2.6) lowers the components of the estimation that are in the larger variance direction. For that reason, we relate it to the norm of the error vector. If we denote  $S = \frac{1}{\sigma_\xi^2}$  and  $T = (\prod_i \lambda_i)^{1/3}$ , which is homogeneous to  $\lambda$ , we finally obtain

$$Q = S \cdot T \quad (19)$$

where  $S$  can be seen as the similarity between both images after deformation, while  $T$  quantifies the amount of texture in the observation window. Indeed, we have

$$S = \frac{1}{\sigma_\xi^2}, \quad (20)$$

where

$$\sigma_\xi^2 = \sum_{x_i \in \Omega} w_i^2 (I_d(x_i) + \alpha \delta I + \nabla I_m(x_i) \cdot \delta \mathbf{x})^2. \quad (21)$$

The quantity

$$-(\nabla I_m \cdot \delta \mathbf{x} + \alpha \delta I)$$

is our model for the difference image  $I_d$ . In Sect. 4, we analyse which part of the observations  $I_d$  is explained by this model, and  $S^{-1}$  is an estimation of the quantity  $\sigma_\xi^2$ . As the noise on images  $I_1$  and  $I_2$  is assumed to be Gaussian white noise  $N(0, \sigma_I^2)$ ,  $\sigma_\xi^2$  can be interpreted as an estimation of  $2\sigma_I^2$ . It is also bounded by the dynamics of the signal.  $T$  corresponds to a “texture” criterion. It is homogeneous with  $\sum I_x^2$ , which indicates that it is high when the texture is well-suited to the motion analysis. It is low when there is a blank-wall effect or a strong aperture. We use the quality criterion for error prediction (see Sect. 3.1). If  $T$  is large, then the quality is high because the texture of the signal enables motion analysis (no aperture problem). The use of least-squares is well-adapted in the case where the residual  $\xi$  is a Gaussian random variable, but it may be not Gaussian for the following reasons:

- non-Gaussian noise implying a non-Gaussian residual distribution (statistical error): e.g. Poisson noise, spatial noise, etc.;
- modelling error (non-zero second or higher-order terms): motions more complex than translation, non uniform intensity variations;
- noise in the matrix  $A$  due to noisy spatial gradient estimations (spatial aliasing),
- noise in temporal derivative measurement due to temporal aliasing.

A possible way to cope with non Gaussian errors in the future is to use robust minimisation, or iterative weighted least-squares.

### 2.2.6. Aperture reduction

We correct for the aperture effects using the ellipse of error dispersion. The  $\mathbf{p}_i$  vectors (in the space of parameters) are the eigenvectors of the matrix  $V_{\delta\theta}$  defined earlier. We apply the following rule

$$\theta \leftarrow \theta - (\alpha_1 \mathbf{p}_1 + \alpha_2 \mathbf{p}_2 + \alpha_3 \mathbf{p}_3)$$

$$\text{where } \alpha_i = \begin{cases} \beta \sigma_\xi^2 / \lambda_i & \text{if } |\theta_i| > \beta \sigma_\xi^2 / \lambda_i \\ 0 & \text{otherwise} \end{cases}$$

where  $\beta$  is an arbitrary parameter that sets the level of constraint we need for the application. A large  $\beta$  will strongly correct the estimations. The aperture effect between two variables (e.g.  $(\delta x, \delta y)$  or  $(\delta x, \delta I)$ ) occurs when there is not a unique solution to solve the linear system. The aperture reduction helps the algorithm to choose the smallest norm solution. In the estimation of loop motions (see Sect. 4.3), this constraint will remove the aperture along the loop, while keeping the component of the motion perpendicular to the loop (parallel to the gradient).

### 2.2.7. Multiscale updating

We use a multiscale implementation to benefit from each scale of observation starting from the coarsest scale. On coarse scales, the number of pixels used in the estimation (number of “observations”) is higher than on finer scales, which ensures a better goodness-of-fit for a given residual than on a smaller scale (or small neighbourhood  $\Omega$ ). The flowchart of the algorithm is shown in Fig. 3. For our applications, we have chosen the set of scales  $s$  to: 16, 12, 8, and 4 pixels. From scale  $s_i$  to scale  $s_{i+1}$ , we propagate the estimation by adding the computed residual to the current parameters:

$$\theta_{i+1} = \theta_i + \delta \theta_i.$$

**Table 1.** Model for error prediction, with the parameters determined by the calibration using synthetic images.

Mode	Parameters of $\text{err}_\rho$ : $c_i$ (first line) and $d_i$ (second line)			Parameters of $\text{err}_{\delta I}$ : $c'_i$ (first line) and $d'_i$ (second line)		
$(\alpha, \beta) = (0.1, 0.1)$	$-6.4 \times 10^{-2}$	$-7.2 \times 10^{-3}$	$-0.504$	$-8.16 \times 10^{-2}$	$-1.1 \times 10^{-2}$	$-2.4 \times 10^{-1}$
	0.17	$2.1 \times 10^{-2}$	$-7.7 \times 10^{-1}$	$8.9 \times 10^{-2}$	$1.7 \times 10^{-2}$	-1.82
$(\alpha, \beta) = (1, 0.5)$	-0.39	1.69	-0.31	-0.054	-0.24	-0.18
	1.63	-4.13	-1.07	0.155	0.73	-2.44

For scale refinement of our quality criterion, we use how the inverse of our quality criterion can be interpreted as the variance of the error vector in the parameter space. Indeed the inverse of  $Q$  can be simply added. The quality is initialised to

$$Q_0 = q_0.$$

The scale updating strategy from larger scale  $s_i$  to lower scale  $s_{i+1}$  is

$$Q_{i+1}^{-1} = Q_i^{-1} + q_{i+1}^{-1};$$

hence,  $Q$  is given by the final formula

$$Q_{\text{final}} = \frac{\prod_i q_i}{\sum_i \prod_{j \neq i} q_j}.$$

In the case where the aperture reduction condition is not satisfied, there is no update whether in parameter estimation or in quality. We are working on a more robust updating formula.

### 2.3. Postprocessing: heliographic coordinate

For the EIT sequences that are full-disc observations, we convert the velocity parameters  $v_x = \delta x / \delta t$  and  $v_y = \delta y / \delta t$  into heliographic coordinates to get the rotation velocity and the meridional velocity. In the applications, we only use the synodic observation. Assuming that the solar corona is spheric with a photospheric (EIT limb) radius  $R$ , we transform the spatial coordinates into heliographic coordinates and invert the following relationships (true if  $\delta \Lambda$  is small)

$$x = R \cos(B) \sin(\Lambda)$$

$$y = R(\sin(B) \cdot \cos(B_0) - \cos(B) \cdot \cos(\Lambda) \cdot \sin(B_0))$$

$$\delta x \simeq R \cos(B) \cos(\Lambda) \cdot \delta \Lambda$$

$$\delta y \simeq R \cos(B) \sin(\Lambda) \cdot \cos(B_0) \cdot \delta \Lambda$$

where  $x$  and  $y$  are the Cartesian coordinates of the plane-of-the-sky with origin at the centre of the disc,  $L$  is the longitude,  $B$  is the latitude, and  $B_0$  is the heliographic latitude of the centre of the solar disc. We obtain the expression of the angular rotation using the time interval  $\delta t$  separating the images  $I_1$  and  $I_2$ :

$$\omega_{\text{rot}}(x, y) = \frac{\delta \Lambda}{\delta t} \simeq \frac{\delta x}{R \cos(B) \cos(\Lambda) \delta t}. \quad (22)$$

## 3. Calibration

### 3.1. Calibration and error prediction using synthetic images

We used synthetic data to predict the error of our estimations of velocity and brightness variation. For a given constraint on the parameters to estimate, the velocity vector and the brightness variation, we generated pairs of images with varying texture and additive noise that perturb the estimation. In doing so, we obtained the empirical relationship between the quality factor  $Q$  to

the estimation error. These empirical rules can be used and interpreted for error prediction: if we know the quality factor of an estimation, we derive the predicted error from the empirical rule. We first model the error parameters in Eqs. (23) and (24):

$$\delta I_{\text{estimated}} = \delta I_{\text{theoretical}} + \delta I_{\text{error}}$$

$$\delta \mathbf{x}_{\text{estimated}} = \delta \mathbf{x}_{\text{theoretical}} + \delta \mathbf{x}_{\text{error}}.$$

We define  $\rho = \|\delta \mathbf{x}_{\text{error}}\|$ . For each couple  $(\delta x_{\text{th}}, \delta I_{\text{th}})$ , where  $\delta x_{\text{th}}$  is translation in one direction with varying amplitude, we find the empirical rules for the errors  $\text{err}_\rho$  and  $\text{err}_{\delta I}$  as functions of  $(\delta x_{\text{th}}, \delta I_{\text{th}})$ :

$$\text{err}_\rho = 10^{b(\delta x_{\text{th}}, \delta I_{\text{th}})} \cdot Q^{a(\delta x_{\text{th}}, \delta I_{\text{th}})} \quad (23)$$

$$\text{err}_{\delta I} = 10^{b'(\delta x_{\text{th}}, \delta I_{\text{th}})} \cdot Q^{a'(\delta x_{\text{th}}, \delta I_{\text{th}})}. \quad (24)$$

Each of these parameters is a function of the parameters to estimate according to the model:

$$a(\delta x_{\text{th}}, \delta I_{\text{th}}) = c_1 \cdot \delta x_{\text{th}} + c_2 \cdot \delta I_{\text{th}} + c_3$$

$$b(\delta x_{\text{th}}, \delta I_{\text{th}}) = d_1 \cdot \delta x_{\text{th}} + d_2 \cdot \delta I_{\text{th}} + d_3$$

$$a'(\delta x_{\text{th}}, \delta I_{\text{th}}) = c'_1 \cdot \delta x_{\text{th}} + c'_2 \cdot \delta I_{\text{th}} + c'_3$$

$$b'(\delta x_{\text{th}}, \delta I_{\text{th}}) = d'_1 \cdot \delta x_{\text{th}} + d'_2 \cdot \delta I_{\text{th}} + d'_3.$$

The parameters found after the calibration are gathered in Table 1. After introducing the parameter  $\alpha$  in Sect. 2.2.5, the brightness variation parameter is measured in pixel. The parameters of the empirical rules (23) and (24) have been found for ground-truth velocity and brightness variation varying from zero to one pixel. In the future, we will study the empirical rule for parameters larger than one pixel. In Sect. 4.1, we use this error model in order to check the correctness of the estimated velocities and brightness variations.

### 3.2. Semi-artificial EIT sequences

We also calibrated our method on semi-artificial solar sequences. We applied a displacement field to an EIT image  $I_1$  and obtained a second image  $I_{1,\text{dr}}$  using the parametric models of rigid and differential rotation estimated by Vršnak et al. (2003). The interpolation procedure is based on the IDL function of cubic interpolation (Park & Schowengerdt 1983). This method uses cubic polynomials to approximate the optimal sinc interpolation function. Due to spatial aliasing, this gives bad results when there are high spatial frequencies since it assumes that the signal is band-limited (Deforest 2004). This effect lowers the similarity term  $S$ , since the image pattern is not correctly deformed, and the simple model of deformation (local translation and constant BV) is no longer valid. The measurements are then projected back into rotational motions and meridional motions. In Fig. 4 we compare the extracted rotation velocity with the curve of the theoretical rotation. Each bin is 0.5 degree-per-day wide and 1 degree in latitude high. The relative dispersion around the theoretical rotation is approximately  $\pm 0.5$  degree-per-day ( $\pm 5\%$ ). This value is to be compared with the dispersion that we find on real sequences (Sect. 4).

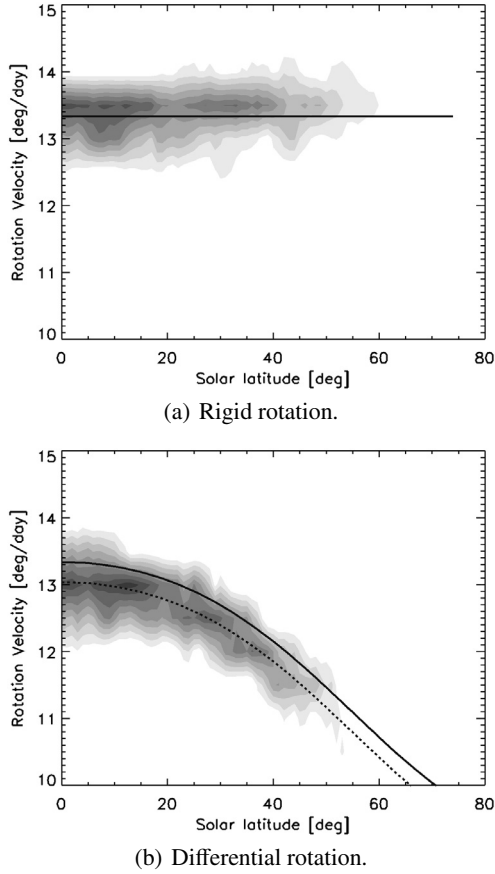


**Fig. 4.** Calibration using *semi-artificial* EIT sequences on which a synthetic rotation has been applied for a rigid rotation (plain line in **a**) and a differential rotation (**b**). Vertical axis: synodic rotation velocity (in degree per day). Horizontal axis: solar latitude (in degree). The grey level represents the density of solar-disc pixels according to their latitude and estimated rotation velocity. In **b**, the plain line represents the differential rotation found by Vršnak et al. (2003). The dotted line follows the maximum density of pixels: it shows that the differential rotation measured by the algorithm has a small bias ( $-0.3$  degree per day).

#### 4. EUV sequence analysis

In this section, we present the processing of three pairs of images:  $(I_1, I_2)$ ,  $(J_1, J_2)$ , and  $(K_1, K_2)$ . The images  $I_1$  and  $I_2$  were observed by EIT on 1999-04-17, respectively, at times 00:00:11 and 00:36:10 in the CME watch mode, at the wavelength 19.5 nm. The second EIT sequence  $(J_1, J_2)$  was observed on 1998-05-03, respectively at times 21:12:09 ( $J_1$ ) and 21:25:35 ( $J_2$ ). We ran the algorithm on rebinned images with a resolution of  $512 \times 512$  pixels. The last sequence is a pair of TRACE images observed on 1998-07-14 at times 12:50:16 ( $K_1$ ) and 12:52:46 ( $K_2$ ) in the 17.1 nm passband, with a resolution of  $768 \times 768$  pixels. EIT images were processed using the `eit_prep` IDL procedure of the SolarSoft and cleaned of cosmic rays. TRACE images were processed using the `trace_prep` IDL procedure of the SolarSoft; they were cleaned of cosmic rays, de-streaked, and derippled.

##### 4.1. EIT sequence 1 (EIT1)

We analysed the rotation on a sequence taken on 1999-04-17 in the EIT 19.5 nm bandpass during a CME Watch observation campaign. The images were observed at 1999-04-17T00:00:11

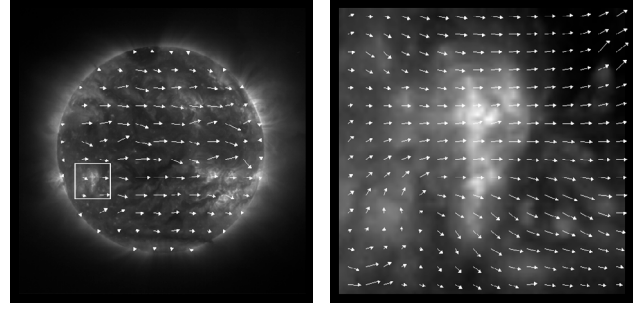


**Fig. 5.** EIT1. *Left*: on-disc subsampled velocity field  $(\delta x, \delta y)$  for the couple of image  $(I_1, I_2)$ . *Right*: zoom showing the active region.

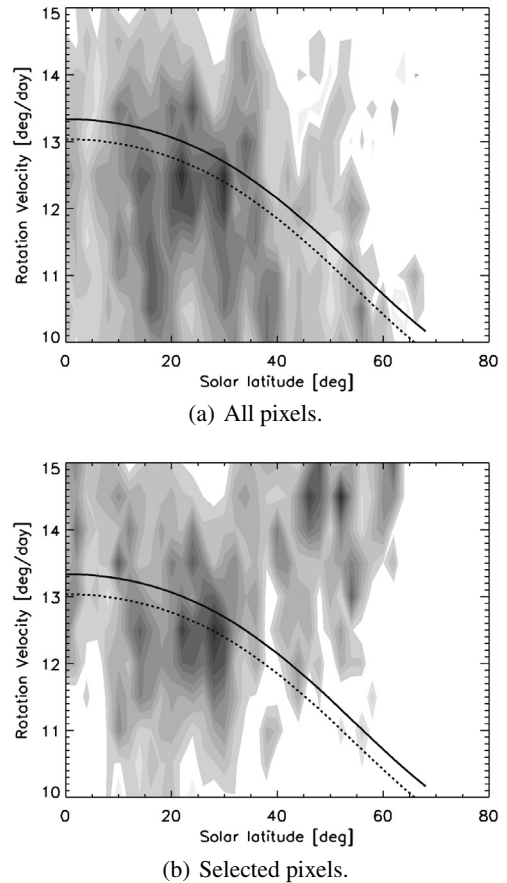


**Fig. 6.** EIT1. **a**): Rotation for all pixels located on the solar disc for  $(I_1, I_2)$ . The grey value represents the density of pixels. There is high variability around the theoretical differential rotation. **b**): Rotation estimated for pixels with a high  $\|\delta \mathbf{x}\|/\|\delta \mathbf{x}_{\text{error}}\|$  ratio ( $>5$ ). In **a**) and **b**), each column (or band of latitude) is normalised so that black means 100% of the latitude band, while white means 0%. The plain line represents the differential rotation found by Vršnak et al. (2003). The dotted line shows the bias found on the semi-artificial EIT sequence. In **b**), the velocity of the estimated pixels has a high level of confidence according to our error prediction. At the highest available latitude ( $>40$  degrees), the rotation velocity of most pixels is higher than expected.

and 1999-04-17T00:36:10. We analyse the sequence  $(I_1, I_2)$  in the same conditions as in Sect. 3. We choose the following parameters:  $\beta = 0.1$  (“weak” aperture reduction) and  $\alpha = 0.1$ . In Fig. 5, the subsampled resulting velocity is displayed. Figure 6a shows the rotation velocity of all on-disc pixels, while in Fig. 6b we select the pixels that have the most reliable estimation ( $\|\delta \mathbf{x}\|/\|\delta \mathbf{x}_{\text{error}}\|$ , see Fig. 7a), according to their latitude

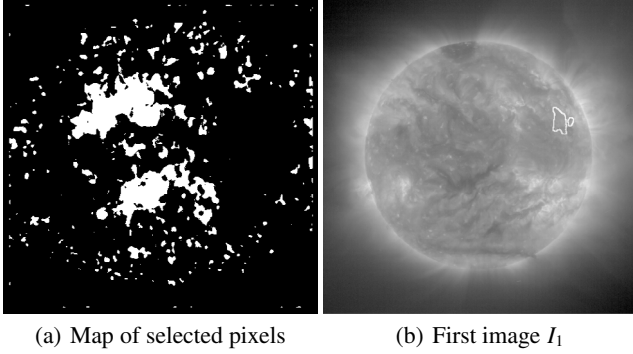


**Fig. 7.** EIT1. *Left:* map of selected pixels according to the criterion  $\|\delta\mathbf{x}\|/\|\delta\mathbf{x}_{error}\| > 5$ . The error prediction ensures that the selected pixels have reliable velocity estimations. *Right:* first image  $I_1$  with two regions R1 and R2 extracted from thresholded BV map  $\alpha\delta I$ .

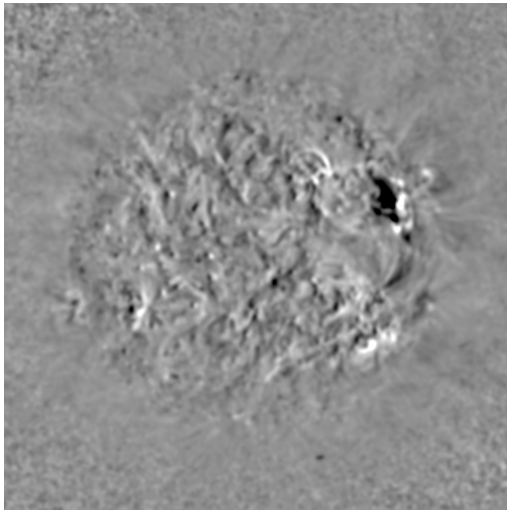


**Fig. 8.** EIT1. Difference image for the sequence  $(I_1, I_2)$  at the 512 pixel resolution. The variance is  $9.2 \times 10^{-4}$  at the 512 pixel resolution, and  $1.8 \times 10^{-3}$  at the 1024 pixel resolution.

and their velocity rotation  $\omega_{rot}$ . The selected pixels are shown in Fig. 7a. We also plot the theoretical rotation (plain line). The estimated velocities are variable (up to  $\pm 2$  degrees per day,  $\pm 15\%$ ). Figure 11 shows the model  $-(\nabla I_m \cdot \delta\mathbf{x} + \alpha\delta I)$  of the difference image  $I_d$  (Fig. 8) that is provided by the algorithm. This model has a variance of  $7 \times 10^{-4}$ , lower than the variance of the difference image ( $9.2 \times 10^{-4}$ ), but it has the same order of magnitude (76% of the difference image variance). The modelled difference image (Fig. 11) is the sum of  $-\nabla I_m \cdot \delta\mathbf{x}$ , caused by the velocity (59% of the difference image variance, see Fig. 9) and of  $-\alpha\delta I$  caused by the brightness variation (42% of the difference image variance, see Fig. 10). Figure 7b shows the two regions R1 (left) and R2 (right) extracted from the thresholded BV map  $\alpha\delta I > 0.14$ . We choose this threshold from analysis of the BV histogram. We use the error prediction to derive the mean values of  $err_{\delta I}$  over regions R1 and R2, which are 0.007 and 0.006, respectively. Finally, we obtain (units are in DN):

$$\begin{aligned} \text{mean}(\text{bv}(R_1)) &= -0.206 \pm 0.006, \\ \text{mean}(\text{bv}(R_2)) &= 0.166 \pm 0.009. \end{aligned}$$

The remaining residual is shown in Fig. 12 (variance:  $9.35 \times 10^{-5}$ ). Furthermore, one can use the BV map (Fig. 10) to study what could be a bright front above the dimming. The positive

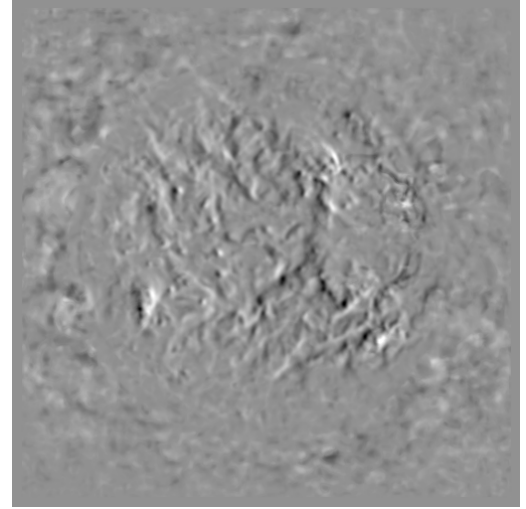


**Fig. 9.** EIT1. Proportion of difference image interpreted as motion for the sequence  $(I_1, I_2)$ . This is the quantity  $-\nabla I_m \cdot \delta\mathbf{x}$  at the 512 pixel resolution. The variance is  $5.4 \times 10^{-4}$ .

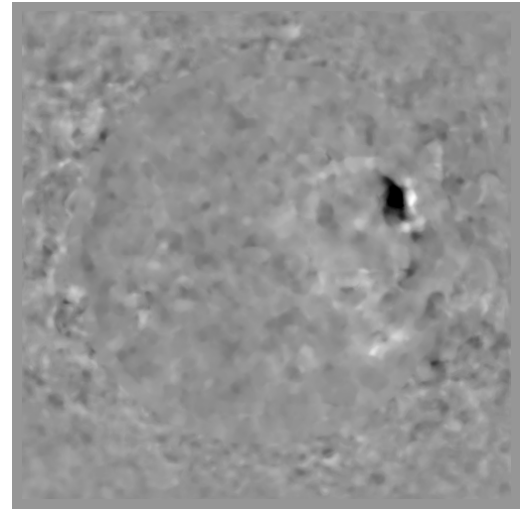


**Fig. 10.** EIT1. Proportion of difference image interpreted as brightness variation for the sequence  $(I_1, I_2)$ . This is the quantity  $-\alpha\delta I$  at the 512 pixel resolution. The variance is  $4.2 \times 10^{-4}$ .

aspect of this technique is that it does not use any compensation for rotation using an interpolation.

At high resolution ( $1024 \times 1024$  pixels), we applied the same algorithm using the same neighbourhood sizes. We found, as expected, that the residual and model maps appear sharper (Figs. 13 and 14). The variance of the model is  $1.4 \times 10^{-3}$ , which is 78% of the difference image variance. The ratios between residual variance and the difference image variance are the same at both resolutions (10%). The sum of the model and the residual explains 86% of the difference image variance at low resolution and 88% at high resolution. The coefficients of correlation between the model and the difference image are the same at both resolutions ( $\rho = 0.95$ ). The coefficient of correlation between the model and the residual is  $\rho = 0.25$  at the 512 pixel resolution, and lower ( $\rho = 0.23$ ) at the 1024 pixel resolution, which confirms a better decomposition of the data  $I_d$  into the model and the residual at high resolution. The algorithm will be applied on full resolution data when the code is optimised (see Sect. 5).

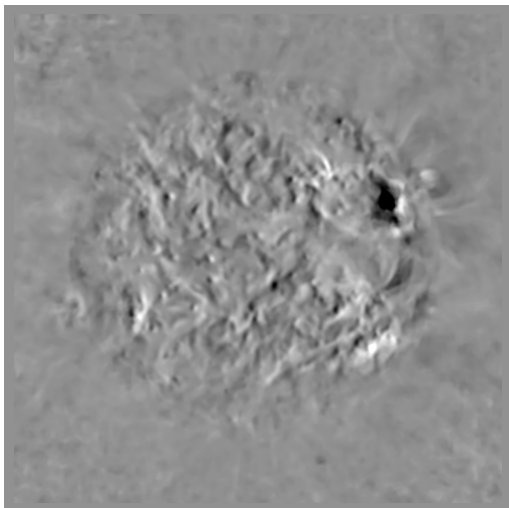


**Fig. 11.** EIT1. Model for difference image  $I_d = I_2 - I_1$ . This is the quantity  $-(\nabla I_m \cdot \delta \mathbf{x} + \alpha \delta I)$  at the 512 pixel resolution. The variance is  $7 \times 10^{-4}$ : the model interprets 76% of the data (the difference image).

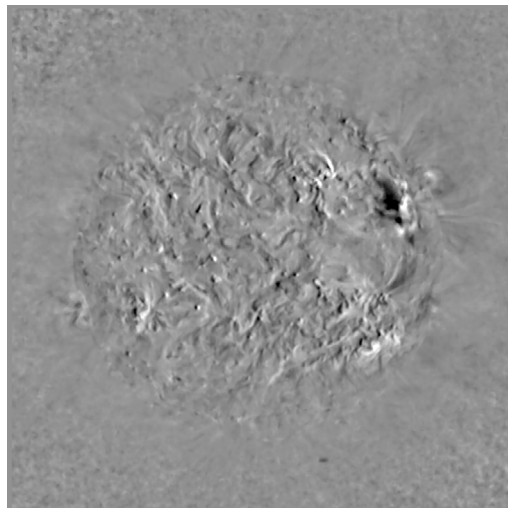


**Fig. 13.** EIT1. Model for difference image  $I_d = I_2 - I_1$ . This is the quantity  $-(\nabla I_m \cdot \delta \mathbf{x} + \alpha \delta I)$ , but in the high-resolution case ( $1024 \times 1024$  pixels). The variance is  $1.4 \times 10^{-3}$  (78% of the difference image variance).

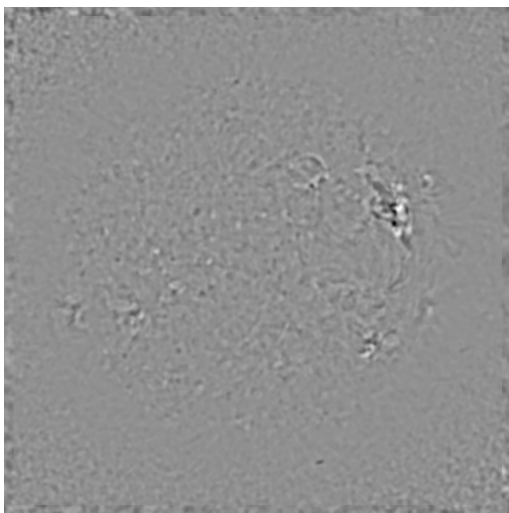


**Fig. 12.** EIT1. Residual for the sequence  $(I_1, I_2)$ . This is the quantity  $I_d + \nabla I_m \cdot \delta \mathbf{x} + \alpha \delta I$  at the 512 pixel resolution. The variance is  $9.35 \times 10^{-5}$ : it means that 10% of the variance of data (the difference image) is interpreted as residual.

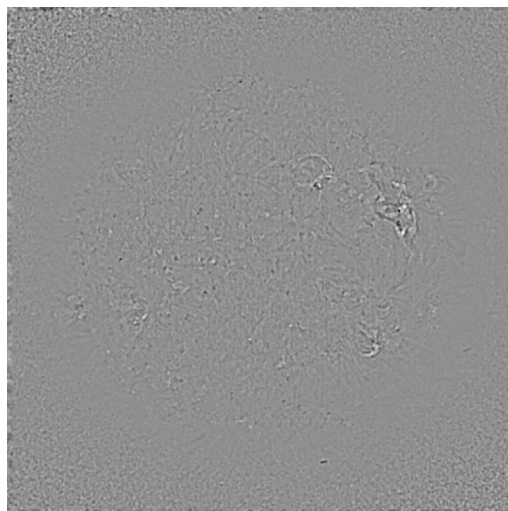


**Fig. 14.** EIT1. Residual for the sequence  $(I_1, I_2)$ . This is the quantity  $I_d + \nabla I_m \cdot \delta \mathbf{x} + \alpha \delta I$ , but in the high-resolution case ( $1024 \times 1024$  pixels). The spatial resolution of the residual is higher than at the 512 pixel resolution. The variance is  $1.8 \times 10^{-4}$  (10% of the difference image variance). The sum of the model and the residual explains 88% of the difference image variance.

#### 4.2. EIT sequence 2 (EIT2)

We analysed a brightness variation occurring on 1998-05-03, at times 21:12:09 ( $J_1$ ) and 21:25:35 ( $J_2$ ) in the CME Watch mode, at the passband 19.5 nm. The original image  $J_1$  is shown in Fig. 15a. In the difference image  $J_d$  (Fig. 15b), there is a strong brightness variation. For this application, we chose the aperture reduction mode:  $\beta = 0.5$  and  $\alpha = 1$ . In the particular region where we focus the study (see Fig. 15a), it appears clearly from both the velocity field (Fig. 16) and the brightness variation map (Fig. 17) that the algorithm is able to carry out a correct interpretation of the difference image, confirmed by a visual inspection. The motion of the loop is detectable in Fig. 16 in the middle of the image. This mode increases the bias, so that the parameters, e.g. the velocity vector, is underestimated. For this reason the predicted error is also pessimistic. Nevertheless it is possible to choose detection thresholds to automatically identify this event. In that case, the full difference image  $J_d$  (Fig. 15b) is only partly explained quantitatively by the model  $-(\nabla J_m \cdot \delta \mathbf{x} + \alpha \delta J)$ : indeed

it represents 44% of the variance of  $J_d$ . Both terms of the model undergo the strong correction that biases the parameters, but here the difference image has been explained mostly by brightness variation.

#### 4.3. TRACE sequence

The TRACE images  $K_1$  and  $K_2$  are observed on 1998-07-14 at times 12:50:16 ( $K_1$ ) and 12:52:46 ( $K_2$ ), respectively. For this application, we chose the strong correction mode:  $\beta = 1$  and  $\alpha = 1$ . It is adapted to measuring the velocities in the normal direction of the loop. The original image with the region of interest is shown in Fig. 18. The global shift motion is estimated with coarse full-image cross-correlation and then introduced as an initial velocity vector to the algorithm. Again, in this case, the difference image (Fig. 19) is not completely explained by the

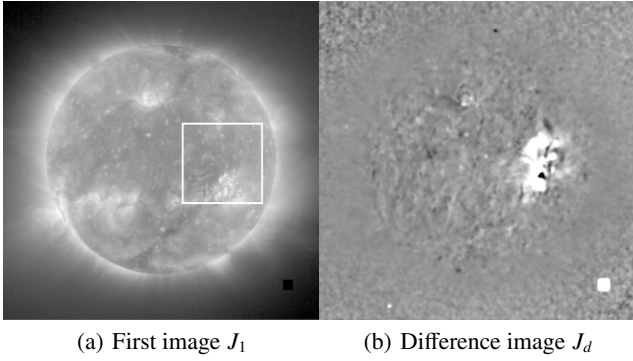


**Fig. 15.** *Left:* first image  $J_1$  showing the location of a strong brightness variation at the 512 pixel resolution. *Right:* difference image  $J_d = J_2 - J_1$  at the 512 pixel resolution. The variance is  $2.94 \times 10^{-3}$ .

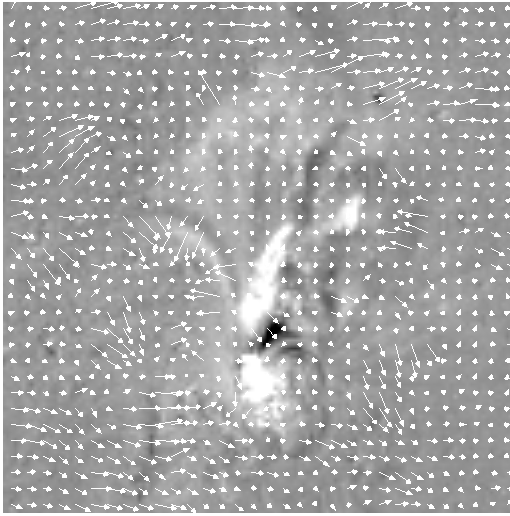


**Fig. 16.** EIT2. Zoom on difference image (no smoothing) with velocity field  $\delta x$  superimposed. The loop motion in the middle of the image can be clearly identified.

model (Fig. 20), which explains 29% of the difference-image variance. The velocity term of the model seems to overlap the moving loops of the active region. The strong aperture reduction mode ensures that these loops are oscillating, although we still have to analyse the error prediction in detail. On the other hand, the brightness variation map covers some part of the active region but also operates over all the Quiet Sun. We focus the study on a region located at the footpoints of the active region loops (Fig. 18). The velocity field superimposed on the difference image is shown in Fig. 21 for this region: the loop oscillation is observable from this sequence of two images. The estimated velocities can be used for detecting and measuring the loop oscillation with precision.

## 5. Discussion of the algorithm

Optical flow estimations using a gradient-based approach have inherent limitations. In particular, strong spatial variations in the signal intensity introduce an error into the gradient computation if the signal is undersampled, and the optical flow estimation may be unstable. In that case, the gradients are dissimilar in both images. The SOFA constraint, which measures the dissimilarity between gradients in both images, will then regularise the estimation (implying  $\delta\theta \rightarrow 0$  in Sect. 2.2.7) to prevent

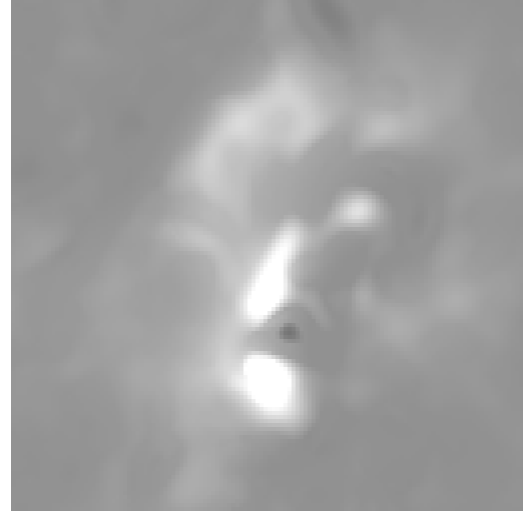


**Fig. 17.** EIT2. Zoom on the brightness variation map  $-\alpha\delta J$ . The brightness variations that dominate in the difference image are correctly identified as such on the brightness variation map.

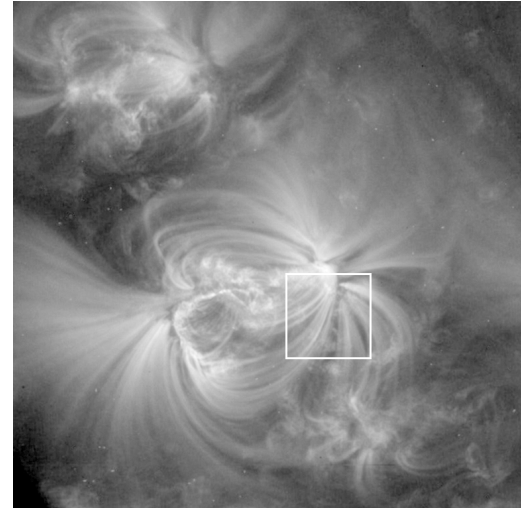


**Fig. 18.** TRACE. Image of  $K_1$  showing the location of the region of interest. The resolution is  $768 \times 768$  pixels.

unstable estimation. In EUV images of the corona, the loops appear smooth, but brightenings or PLS present strong small-scale intensity variations that may suffer from this effect in the optical flow estimation.

The requirement on the spatial resolution is given by the smallest neighbourhood  $\Omega$  of the multiscale process. If there are several moving objects smaller than the lowest scale (4 pixels here) within the neighbourhood, the estimated motion will be a “mean motion” of these objects.

The requirement on the temporal resolution is given by the maximum size of the vector that can be estimated. Indeed if the optical flow vector to estimate is too large, the spatial gradients at a given pixel location in  $I_1$  and  $I_2$  will differ. The condition on the maximal movement measured by a gradient-based OF approach is that, over the displacement range  $\delta x$ , the slope  $\nabla I$  must be uniform; in other words, this condition of gradient uniformity ensures that the second-order (Hessian matrix, see Appendix A), and even higher-order, terms of the OF residual vanish over the displacement range. If the motion is too large, and the gradients of both successive signals are different, the symmetry constraint

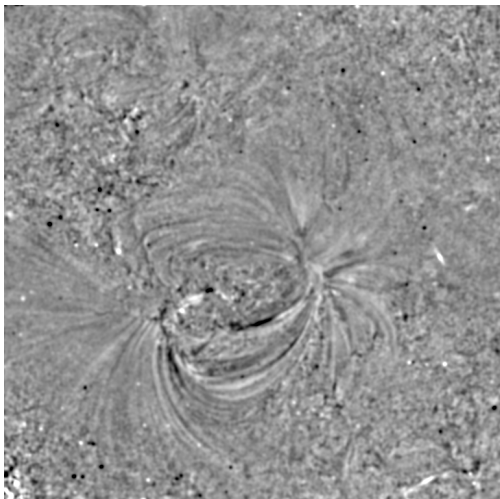


**Fig. 19.** TRACE. Difference image  $K_d = K_2 - K_1$ . The variance is  $1.36 \times 10^{-3}$ .

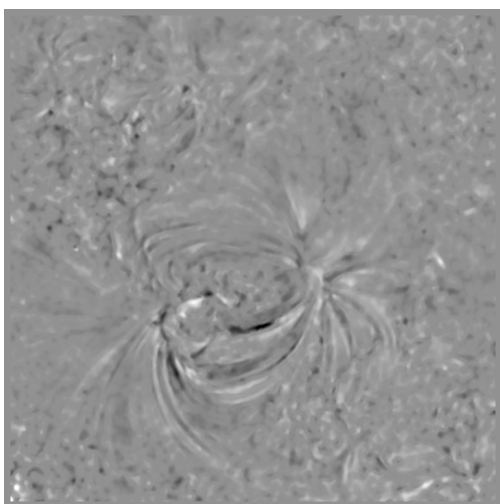


**Fig. 20.** TRACE. Model of difference image  $K_d = K_2 - K_1$ . This is the quantity  $J_d + \nabla J_m \cdot \delta x + \alpha \delta J$ . The variance is  $4 \times 10^{-4}$ .

will again penalise the optical flow estimation thereby preventing unstable computation.

There is no such condition on the brightness variation estimation, and the only encountered limitation occurred on small-scale and strongly-peaked brightness variations. This is due to the size of the smallest neighbourhood, which is too large for such variations. Unfortunately, we cannot use smaller neighbourhoods since the variance estimation then becomes too high (too few pixels, i.e. too few equations in the linear system). It is possible that the aperture reduction permits use of even lower neighbourhood size, but it has not been assessed yet.

Algorithms exist that extend optical flow to more than two images, but we think that it is better to choose the simplest motion model (local translation over the time difference gap, 12 min in the case of EIT images), as we did, and to post-process the results to build trajectories, by linking the successive displacements when they are reliable.

In the case of rebinned  $512 \times 512$  pixel images, the computation time of the IDL code is 300 s on a Optron 850 (2.4 GHz) processor. In the case of the high-resolution image ( $1024 \times 1024$  pixels), the same computation lasts 1400 s. In the TRACE example, we work at the original resolution

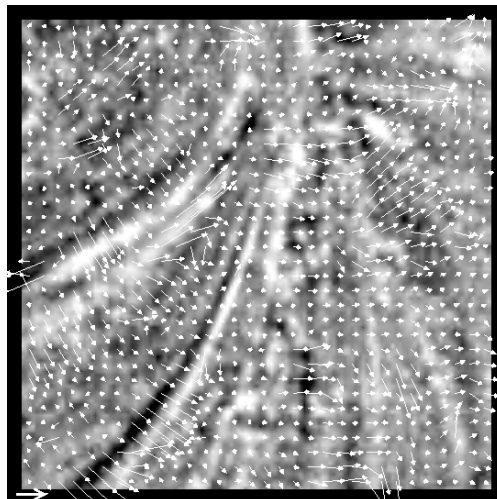


**Fig. 21.** TRACE. Zoom on the region of study for the sequence  $(K_1, K_2)$ . The subsampled velocity field is superimposed on the difference image. The arrow in the lower left corner represents a displacement of one pixel.

( $768 \times 768$  pixels) and the computation time is 740 s. The algorithm has not been optimised yet. There are several possibilities for optimisation: C++ implementation with optimisation of memory usage, downsampling at higher scales, etc.

## 6. Conclusion

We have demonstrated the ability of our optical flow algorithm to interpret the difference image of a sequence of two EUV images as the sum of two components, one due to the motion and the second due to the brightness variation of the moving objects. Real and semi-artificial EIT sequences have been analysed in terms of motion and brightness variations over the full solar image. A multiscale implementation refining the estimation from coarse scale to fine scales enables us to cope with complex motions. The estimation is dense (one estimation for each pixel), and the algorithm provides a quality map, which is related to the error maps. This quality factor has been calibrated on synthetic images with ground truth of the parameters, and this calibration has given empirical rules for error prediction. The calibrated error helps in reliably distinguishing moving objects and appearance/disappearance of coronal structures in a sequence of EUV images. The model for the difference image can be used for event detection. An event can be defined as a particular motion (e.g. a loop motion in the sequence  $(J_1, J_2)$ ) or a strong brightness variation  $-\alpha \delta J$ . In the velocity maps, we observed accumulations of pixels into clusters that have a common rotation velocity. In a future work, we will study the variability in the rotation velocity of, e.g., an active region over half a rotation, which will be possible after processing longer sequences. We plan to analyse the trends of the differential rotation over the solar cycle. Also, investigating the BV maps will allow for a better understanding of the weak dimmings and brightenings, which are concurrent with the fast motion but are merged in the difference image.

This algorithm is a scientific data-analysis tool that provides the apparent velocities and the brightness variation of any coronal events on the difference-image time scale. For instance, the processing of a long sequence will provide precise measurements of the loop oscillations observed in TRACE data. The algorithm also has the potential to achieve automatic event

detection: e.g., it can become a routine of oscillation detection. Automatic detection of events in sequences of two coronal EUV images can also be achieved using the BV maps, such as in the sequence of 1999-04-17 (EIT1): a brightening covering a large area has been unambiguously singled out from the regular solar signal. Moreover, we want to investigate the correlations in time between our events (fast motions, strong brightness variations), their localisations, and high corona signals (LASCO CMEs and in-situ ACE data).

Ultimately, the software will achieve online computation and automatic interpretation of EUV movies of the solar corona, and the outputs will be ready to be assimilated by physical models and data assimilation processes. The presented optical flow algorithm leads to solar physics research, as well as to real-time space weather services. A website describes the recent and updated results: <http://www.sidc.be/velociraptor>.

*Acknowledgements.* The authors acknowledge Véronique Delouille, Eva Robbrecht, Susanna Parenti, Matthieu Kretzschmar, Gareth Lawrence, Laurent Jacques, Valérie Charoing, Françoise Dibos, and Jean-Pierre Antoine for interesting discussions. The authors also acknowledge the support from the Belgian government through PRODEX. Effort has also been sponsored by the Air Force Office of Scientific Research, USA, under grant number FA8655-05-1-3021. SOHO is a project of international cooperation between ESA and NASA.

## Appendix A: PDE formulation of the optical flow

The PDE approach considers the image intensity  $I(\mathbf{x}(t), t)$  as a physical quantity that is conserved over time, where  $\mathbf{x} = (x, y)^T$  is the spatial position in the image plane. The PDE form of the BCA is:

$$\frac{dI}{dt} = 0. \quad (\text{A.1})$$

The differentiation of  $I(\mathbf{x}(t), t)$  in Eq. (A.1) gives the OFCE:

$$\nabla I \cdot \mathbf{v} + \frac{\partial I}{\partial t} = 0, \quad (\text{A.2})$$

where  $\mathbf{v} = (dx/dt, dy/dt)^T$  is the velocity vector of the apparent motion. As the real signals are discrete, the temporal and spatial derivatives must be approximated. We hereafter use the finite difference scheme to compute the *temporal* derivative  $\partial I/\partial t$  using the difference image  $\delta I = I_2 - I_1$  and the time distance  $\delta t$  between  $I_1$  and  $I_2$ :

$$\frac{\partial I}{\partial t} = \lim_{\Delta t \rightarrow 0} \frac{I(\mathbf{x}, t + \Delta t) - I(\mathbf{x}, t)}{\Delta t} \simeq \frac{\delta I}{\delta t} + o\left(\delta t \frac{\partial^2 I}{\partial t^2}\right).$$

From Sect. 2.1, we know the analytical expression of the gradient, given by:

$$\nabla I = \left( \frac{\partial g_a}{\partial x} \star I, \frac{\partial g_a}{\partial y} \star I \right)^T.$$

The discrete OFCE is:

$$\nabla I \cdot \mathbf{v} + \frac{\delta I}{\delta t} = \xi(\mathbf{x}, \delta t), \quad (\text{A.3})$$

where  $\delta I = I_2(\mathbf{x}) - I_1(\mathbf{x}) = g_a \star \delta I$ .

The order of the discretization error (different from the model error) is (see Press et al. 1992):

$$\xi(\mathbf{x}, \delta t) \sim \delta t \frac{\partial^2 I}{\partial t^2}.$$

In this first approach, the spatial derivatives can be computed from either image  $I_1$  and/or  $I_2$ . In the case of formulation of image registration, the order of error due to the truncation of higher order terms is:

$$\xi(\mathbf{x}, \delta \mathbf{x}) \sim \delta \mathbf{x}^T H_I \delta \mathbf{x},$$

where  $H_I$  is the Hessian matrix of  $I$ .

## References

- Barron, J., Fleet, D., Beauchemin, S., & Burkitt, T. 1992, CVPR, 92, 236  
 Black, M., & Anandan, P. 1993, in ICCV93, 231  
 Brajša, R., Wöhl, H., Vršnak, B., et al. 2001, A&A, 374, 309  
 De Groof, A., Berghmans, D., van Driel-Gesztelyi, L., & Poedts, S. 2004, A&A, 415, 1141  
 Deforest, C. E. 2004, Sol. Phys., 219, 3  
 Deforest, C. E., & Gurman, J. B. 1998, ApJ, 501, L217  
 Delaboudinière, J.-P., Artzner, G. E., Brunaud, J., et al. 1995, Sol. Phys., 162, 291  
 Gissot, S. F., Hochedez, J.-F., Dibos, F., et al. 2003, in Solar Variability as an Input to the Earth's Environment, ESA SP-535, 853  
 Handy, B. N., Acton, L. W., Kankelborg, C. C., et al. 1999, Sol. Phys., 187, 229  
 Hochedez, J. F., Zhukov, A., Robbrecht, E., et al. 2005, Ann. Geophys., 23, 3149  
 Horn, B., & Schunck, G. 1981, Artificial Intelligence, 17, 185  
 Hudson, H. S., & Cliver, E. W. 2001, J. Geophys. Res., 25199  
 Klimchuk, J. A., Tanner, S. E. M., & De Moortel, I. 2004, ApJ, 616, 1232  
 Krijger, J. M., & Roudier, T. 2003, A&A, 403, 715  
 Krijger, J. M., Roudier, T., & Rieutord, M. 2002, A&A, 387, 672  
 Kucera, T. A., Tovar, M., & De Pontieu, B. 2003, Sol. Phys., 212, 81  
 Longcope, D. W. 2004, ApJ, 612, 1181  
 Lucas, B., & Kanade, T. 1981, in IJCAI81, 674  
 Moses, D., Clette, F., Delaboudinière, J.-P., et al. 1997, Sol. Phys., 175, 571  
 Noglik, J. B., Walsh, R. W., & Ireland, J. 2005, A&A, 441, 353  
 November, L. J., & Simon, G. W. 1988, ApJ, 333, 427  
 Odobez, J.-M., & Bouthemy, P. 1995, J. Visual Commun. Image Representation, 6, 348  
 Oraevsky, V. N., & Sobelman, I. I. 2002, Astron. Lett., 28, 401  
 Park, S., & Schowengerdt, R. 1983, Computer Vision, Graphics & Image Processing, 23, 256  
 Periaswamy, S., & Farid, H. 2003, IEEE Transactions on Medical Imaging, 22, 865  
 Peter, H., Gudiksen, B. V., & Nordlund, Å. 2006, ApJ, 638, 1086  
 Press, W. H., Teukolsky, S. A., Vetterling, W. T., & Flannery, B. P. 1992 (Cambridge: University Press)  
 Roudier, T., Rieutord, M., Malherbe, J. M., & Vigneau, J. 1999, A&A, 349, 301  
 Schrijver, C. J., Title, A. M., Berger, T. E., et al. 1999, Sol. Phys., 187, 261  
 Simoncelli, E. P. 1999, in Handbook of Computer Vision and Applications, ed. B. Jähne, H. Haussecker, & P. Geissler (San Diego: Academic Press), 2, 397  
 Simoncelli, E. P., Adelson, E. H., & Heeger, D. J. 1991, in Proc. Conf. on Computer Vision and Pattern Recognition (Maui, Hawaii: IEEE Computer Society), 310  
 Vršnak, B., Brajša, R., Wöhl, H., et al. 2003, A&A, 404, 1117  
 Welsch, B. T., Fisher, G. H., Abbett, W. P., & Regnier, S. 2004, ApJ, 610, 1148